



Quasi-bound states in the continuum-based switchable light-field manipulator

RUN CHEN,¹ TIANYUE LI,¹  QIANHUI BI,¹ SHUMING WANG,^{1,2,*}
SHINING ZHU,^{1,2} AND ZHENLIN WANG¹

¹National Laboratory of Solid-State Microstructures, Collaborative Innovation Center for Advanced Microstructures, School of Physics, Nanjing University, Nanjing, 210093, China

²Key Laboratory of Intelligent Optical Sensing and Manipulation Ministry of Education, Nanjing 210093, China

*wangshuming@nju.edu.cn

Abstract: Nonlocal metasurfaces, which support a collective mode, can be applied to manipulate the wavefront within the narrow band spectrum and do not operate other wavelengths. However, once fabricated, the tunability of those meta-devices is still a challenge. Here, we demonstrated a switchable all-dielectric nonlocal metasurface based on quasi-bound states in the continuum controlled by symmetry breaking. This device realizes the spatial light beam manipulation in the narrow band with switchable resonant wavelengths in different environment dielectric. We designed a nonlocal metasurface for beam focusing with a tunable wavelength in the communication band. We also designed a nonlocal metasurface for the generation of non-diffraction Airy beams with tunable wavelength. These results will have potential applications in see-through display, large-capacity optical communications, nonlinear optics and imaging.

© 2022 Optica Publishing Group under the terms of the [Optica Open Access Publishing Agreement](#)

1. Introduction

The emergence of metasurface opens up a decade of innovation in Nano-photonics, such two-dimensional (2D) optical element consists of the array of well-designed sub-wavelength scatterers, which possesses an ability to manipulate the light field [1]. There are two typical metasurfaces in general duo to light-scatterer interaction. One is called local metasurface, composed of unit-cells that are only regarded as each individual nano-antenna without the interaction between the field of adjacent unit-cells [2], which can be extensively applied in manipulating the polarization, phase and amplitude of the light and implemented functions like imaging [3–5], displaying [6–8] and structured light generation [2,9–13] and quantum source [14,15]. The other is defined as nonlocal metasurfaces supporting a collective mode, such as Fano resonance or guided mode resonance [16–19]. Compared with local metasurfaces, nonlocal metasurfaces have an outstanding feature to manipulate light field within a narrowband spectrum near the resonant frequency without other optical response in extra wavelengths. Recently, some pioneering works related to nonlocal metasurface have been reported, such as beam deflection and focusing [17,20].

On the other hand, tunability of metasurfaces is always the topic of people's concern. A lot of efforts have been made on local metasurfaces [21–23]. For nonlocal metasurface, recent studies have realized that tunable resonance frequency on nonlocal metasurface arising from thermo-optic effects [24]. In photonics crystal (PhC) slabs, there is a special collective mode named bound states in the continuum (BIC). They are completely bounded in the PhC slabs in spite of their momenta and energies matching the free space plane waves. By means of appropriate symmetry-breaking in PhC slabs, the quasi-BIC mode can be formed, which is a kind of Fano resonant mode with a high quality factor (Q-factor) [25,26]. The Q-factor and the resonant wavelength of quasi-BIC mode are closely related to symmetry-breaking and the refractive index of the substrate [27,28]. With this principle, the resonant wavelengths of the designed nonlocal metasurfaces can be shifted in different surroundings.

Here, we propose a method to show the switchable all-dielectric nonlocal metasurfaces empowered by quasi-BIC. By means of the geometric phase supported by quasi-BIC mode, the device possesses the ability to manipulate the spatial light beams. We numerically demonstrate the device by designing three typical wavelength-switchable spatial light modulators in a narrow communication wavelength range, those are, a beam deflector, a focusing device and an Airy beam generator. We envision that our study may be a candidate for the next generation of multifunctional nanophotonic device, ranging from imaging, optical trapping to large-capacity optical communication.

2. Quasi-BIC supported in PhC slabs with period-doubling perturbation

In a four-fold rotational-symmetric PhC slabs system, doubling the period of the PhC slabs are used to construct the quasi-BIC mode. Figure 1(a) illustrates the schematic of the real-space structure (the left side) and the First Brillouin zone (FBZ) in momentum space (the right side) of the unperturbed PhC slabs. Figure 1(b) shows the schematic of the real-space structure (the left side) and the FBZ in momentum space (the right side) of the perturbed PhC slabs. The red area represents the silicon film and white circles are the etched holes. Γ , X and M are the lattice points in the reciprocal space. As shown in the left side of Fig. 1(b), by changing the two adjacent circular holes in the y direction into two elliptical holes with major axes perpendicular to each other (blue dashed boxes), the real-space lattice period in this direction is doubled and the FBZ is reduced to half of the original one in the momentum space. Due to the periodic perturbation, the X point of the unperturbed FBZ fell to the Γ point.

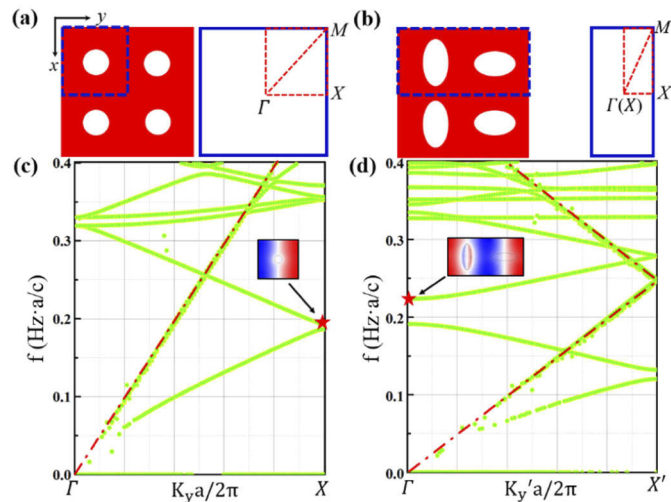


Fig. 1. Schematic of the PhC slabs before and after period-doubling perturbation and their corresponding simulated band structure. The left side of (a) and (b) represent the real-space structure of the unperturbed and perturbed PhC slab respectively. The red area represents the silicon film, and the white area is the etched hole. The blue dashed box is the unit-cell of the lattice in the real space. The right part of (a) and (b) represent the FBZ in momentum space of unperturbed and perturbed PhC slab respectively. Γ , X and M are the lattice points in the reciprocal space. (c) and (d) respectively depict the simulated band structure of unperturbed and perturbed PhC slabs, in which the red dashed line represents light cone. Inset: the modes indicated by the red stars, and their out-of-plane component of electric field is indicated by red and blue.

The Finite-Difference Time-Domain (FDTD) method is performed to simulate this PhC slab before and after perturbation by using the commercial software package “FDTD Solutions”

(Lumerical Inc.). In the simulation, the diameter of the circle is set as 80 nm. The major axis of the ellipse is 300 nm and the minor axis of the one is 80 nm. The index of silicon film is $n_{Si} = 3.45$. Figure 1(c) and Fig. 1(d) show the simulated band structure of the PhC slabs represented by green line before and after perturbation respectively. The red dotted line represents light cone, $\omega = ck_y$. From these two figures, one can see that after such a perturbation, the band structure is folded, and the original bound state mode at X point (the mode indicated by the red star in Fig. 2(c), and the illustration shows the out-of-plane (z direction) electric field distribution of the bound state) falls to the Γ point. This mode changes from a mode under the original light cone to a mode above the light cone, forming a quasi-BIC mode (the mode indicated by the red star in Fig. 1(d), and the illustration shows the out-of-plane electric field distribution of the bound state).

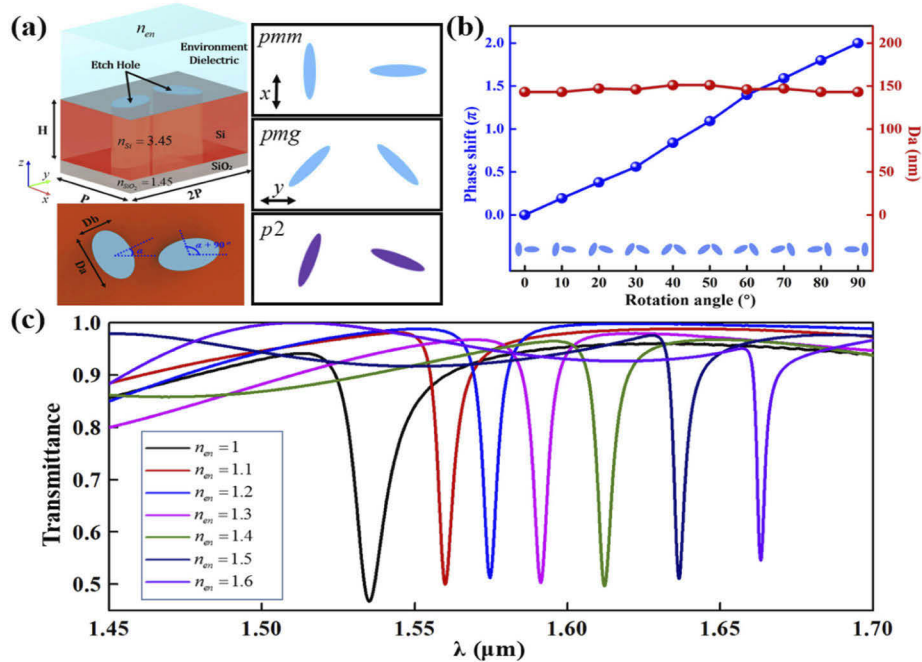


Fig. 2. (a) The left column is the schematic of the unit-cell of designed nonlocal metasurfaces (the top side is the perspective view and the down side is the top view). The right column shows the generation of $p2$ space group. The double handed arrows represent the coupling polarization of pmm and pmg space group. (b) shows the geometric phase of unit-cells. The blue solid line represents the curve of the geometric phase of the unit-cells with the rotation angle. The red curve represents the length of the major axis D_a of the elliptical hole corresponding to rotation angle. The ellipse pairs at the bottom of the image indicate different rotation angle. (c) plots the transmission spectrum when the LCP light incident the unit-cells under different environmental refractive indexes.

3. Unit-cell library and the tunability of the nonlocal metasurface

According to the selection rules for quasi-BIC [29], The polarization direction of the quasi-BIC mode coupling to the free space can be determined. As shown in the right column of Fig. 2(a), the pmm space group and pmg space group are chosen as the parent groups, whose polarization direction coupled with free space is along the x direction and y direction respectively. By arbitrarily rotating the elliptical cylinder by the angle α , the child space group $p2$ can be obtained.

The angle between the polarization direction of the space group coupling to the free space and the x axis is ϕ . When $\alpha = 0$, the $p2$ space group is transformed into the pmm space group, and when $\alpha = \pi/4$, the $p2$ space group is transformed into the pmg space group. From pmm to pmg , ϕ changed $\pi/2$ and α changed $\pi/4$, that is, $\phi = 2\alpha$. This form makes it easy to think of the well-known geometric phase. Actually, when left handed polarized (LCP) light illuminates the system, the phase of left handed polarized (LCP) component and right handed polarized (RCP) component satisfy the following rule [29]:

$$\Phi_{RCP}^r = 0, \quad (1a)$$

$$\Phi_{LCP}^r = 4\alpha, \quad (1b)$$

$$\Phi_{RCP}^t = 4\alpha + \pi, \quad (1c)$$

$$\Phi_{LCP}^t = 0, \quad (1d)$$

where Φ_{RCP}^r and Φ_{LCP}^r are the phase of RCP component and LCP component in reflection side respectively, Φ_{RCP}^t and Φ_{LCP}^t are the phase of RCP component and LCP component in transmission side respectively. As can be seen from the above relation, a geometric phase is imparted as the rotating angle changes, and the phase of RCP light in transmission and LCP light in reflection will vary as four times of rotating angle, for LCP incidence.

With the above principles, a library of unit-cells can be built for the nonlocal metasurfaces. The left side of Fig. 2(a) shows the schematic diagrams of the unit-cells. The fused quartz substrate (the gray layer) is coated with silicon film (the red layer) with height $H = 250$ nm. The refractive index of the Si film is $n_{Si} = 3.45$, and the refractive index of the glass substrate is $n_{SiO_2} = 1.45$. Elliptical cylindrical holes with a height H are etched on the silicon film, and the angle between the major axis directions of the two adjacent ellipses in the y direction is 90° . The period in the x direction is $P = 400$ nm, and the period in the y direction is $2P$. The light blue square above the structure represents the surrounding, such as air, water, etc. For clarity, a top view of the unit-cell is shown in the bottom left of Fig. 2(a). The minor axis of the ellipse is $D_b = 80$ nm, which is equal to the diameter of the circle of the unperturbed photonic crystal slab. The length of the major axis of the ellipse is $D_a = D_b + \delta$, where δ is the perturbation factor. When the LCP light irradiates the unit structure from the substrate, the phase of the transmitted RCP light changes with the rotation angle α as shown in Fig. 2(b). For different α , the resonant wavelength will be slightly different. In order to keep the same resonant wavelength for different α , the size of the major axis D_a of the ellipse has been adjusted appropriately shown as the red curve in Fig. 2(b). When α changes from 0° to 90° , the phase of the RCP light changes from 0 to 2π , indicating a geometric phase relationship of 4 times the rotation angle.

The quasi-BIC mode enhances the interaction between the light and the matter as a result of the high Q-factor. In another hand, this mode is sensitive to the optical properties of matters, such as refractive index. When the surrounding medium is changed, the refractive index of the etched hole will be changed, and the resonant wavelength of quasi-BIC mode will shift. Figure 2(c) depicts the transmission spectrum of the unit-cell in various environmental dielectric with LCP light incidence. The color solid curve is the transmission spectrum under the refractive index of different environmental dielectric over the communication regime. As the refractive index of the environmental dielectric changes from 1 to 1.6, the resonance wavelength shifts from $1.45 \mu\text{m}$ to $1.66 \mu\text{m}$.

4. Design principle of the nonlocal metasurface

4.1. Switchable light deflection on a nonlocal metasurface

Applying the above rules, a nonlocal metasurface with a gradient distribution of rotation angle of 10° has been designed as shown in Fig. 3(a), 19 unit-cells are arranged in a gradient in the x

direction, forming a super-unit-cell with the period of $2P$ in the y direction and the period of $19P$ in the x direction.

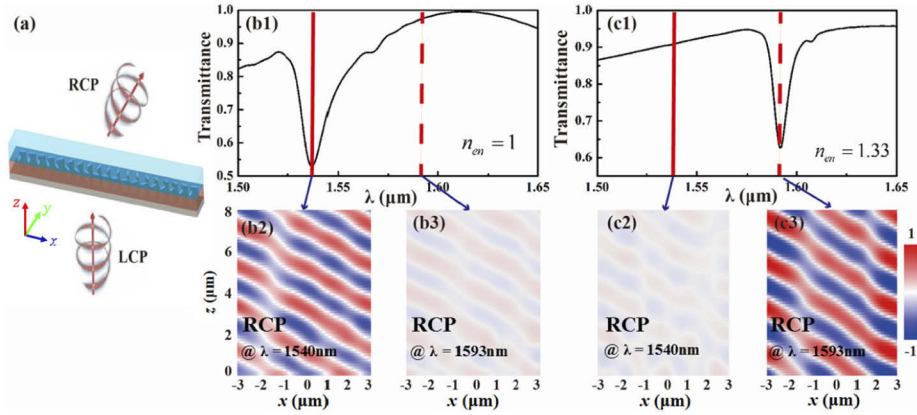


Fig. 3. (a) draws a schematic diagram of a super-unit-cell with 19 unit-cells. The light blue cuboid on the top of the device represents the environmental dielectric. (b1) and (c1) shows the transmission spectra of the LCP light incident from the substrate of the super-unit-cell in the air environment and the water environment, respectively. (b2) and (b3) show the electric field distribution of RCP component of transmission light at 1540 nm (resonant wavelength) and 1593 nm (non-resonant wavelength) in the air environment respectively. (c2) and (c3) show the electric field distribution of RCP component of transmission light at 1540 nm (non-resonant wavelength) and 1593 nm (resonant wavelength) in the water environment respectively.

Based on the generalized Snell's law [1], when LCP light is incident, the wavefront of RCP is transformed at the resonance wavelength under the modulation of the geometric phase. Figure 3(b1) shows the transmission spectrum of the supercell when the surrounding refractive index $n_{en} = 1$ (in the air), and the resonance wavelength is 1540 nm. At this wavelength, the phase of the RCP light changes gradient along the x direction, and the propagation direction of RCP component of transmitted light is deflected by 40° , as shown in Fig. 3(b2). While, in Fig. 3(b3), the amplitude of the electric field of the RCP component is small at the non-resonant wavelength of 1593 nm. The conversion efficiency of right-handed circularly polarized light is low, and the light field is almost uncontrolled by the geometric phase coded in the super-unit-cell. If we place the device in an environment with a refractive index $n_{en} = 1.33$, such as water, the resonant wavelength of the quasi-BIC mode will red shift.

As shown in Fig. 3(c1), the transmission spectrum shows that the resonance wavelength shifts from 1540 nm to 1593 nm. Figure 3(c3) shows that the RCP light is deflected by an angle of 40° at the resonance wavelength of 1593 nm, when the LCP light is incident. Figure 3(c2) shows the amplitude of the electric field of RCP component of transmitted light. It indicates that the conversion efficiency of the RCP light is low, and propagation direction of the light field is almost unaffected at non-resonant wavelength of 1540 nm.

4.2. Switchable nonlocal metasurface for light focusing

In this section, we design a tunable nonlocal metasurface for narrow band focusing. Therefore, the typical phase profile follows:

$$\varphi(r) = -\frac{2\pi}{\lambda_0} \sqrt{(r^2 + f^2)} - f, \quad (2)$$

where $r = \sqrt{x_0^2 + y_0^2}$ is the distance from arbitrary position (x_0, y_0) , λ_0 is the design wavelength, and f_0 is the focal length. For a proof-of-concept, here we simulated one-dimensional device along x direction. This phase profile is coded into the device via rotation of elliptical cylinder of unit-cells at a given coordinate x .

As a result, Fig. 4(a) depicts the nonlocal metasurface for space light focusing. The transmitted RCP component light is focused at different wavelength with LCP light normal incidence in different environment. Figure 4(b) plots the phase distribution for focusing in the x direction, and each dark green sphere corresponds to a unit-cell of the nonlocal metasurface. According to the 4-times relationship between the geometric phase and the rotation angle in the nonlocal metasurface, the rotation angle of the unit-cell is quarter of the corresponding phase. The length of the device in the x direction is 40 μm , and the focal length is set to 16 μm . When the surrounding refractive index $n_{en} = 1$, the LCP is incident from the glass substrate, and its transmission spectrum is plotted in Fig. 4(c1). The resonant wavelength of the device is located at 1540 nm. Figure 4(c2) shows the normalized intensity of the transmitted RCP component light field at the resonant wavelength of 1540 nm. As the result of the modulation of the geometric phase, the light field is focused at this wavelength. At the 1610 nm wavelength away from the resonant peak, as shown in Fig. 4(c3), the light field focus is not formed. If the refractive index of the environment where the device is located is $n_{en} = 1.33$, such as water, the simulated transmission spectrum is plotted in Fig. 4(d1). As the result of the variation of the environment, the resonant peak is red-shifted from 1540 nm to 1610 nm. Figure 4(d2) shows the normalized intensity distribution of the transmitted RCP light at 1540 nm. The original focused image has disappeared. Figure 4(d3) shows the normalized intensity distribution of the transmitted RCP light at 1610 nm. From this image, we can see that the focusing phenomenon previously located at 1540 nm moves to 1610 nm. As can be seen from these images, the focus effect of the light waves remains stable after the change of surrounding medium index. So far, we have realized the design of the frequency-adjustable focusing non-local metasurface.

4.3. Tunable nonlocal metasurface for the generation of Airy beams

Airy beam as a set of solution of the Schrödinger equation exhibits characteristics of the non-diffracting, self-healing and self-accelerating [30,31], have widely inspired the applications including imaging [32,33] and optical communication in medium changing [34,35] or long-distance transmission situation [36]. The electric field envelope of the Airy beam with limited energy can be expressed as:

$$\phi(\xi, x) = Ai \left[bx - \left(\frac{\xi}{2} \right)^2 + ia\xi \right] \exp \left[ax - \left(\frac{a\xi^2}{2} \right) - i \left(\frac{\xi^3}{12} \right) + i \left(\frac{a^2\xi}{2} \right) + i \left(\frac{x\xi}{2} \right) \right], \quad (3)$$

where, $Ai(\cdot)$ is the Airy function, x is the transvers coordinate, b is the transvers scale, ξ is the normalized propagation distance, and a is the attenuation coefficient introduced to obtain the limited energy Airy beam, and here we set it to $a = 0.05$. Let $\xi = 0$, the initial electric field envelope of the Airy beam $\phi(\xi = 0, x) = Ai(bx)\exp(ax)$, The phase distribution along the x direction is $\varphi_{Airy}(x) = \arg[\phi(\xi = 0, x)]$. If we want the airy beam to have any deflection angle, we can add a deflection phase to this phase:

$$\varphi_D(x, \theta) = -\frac{2\pi}{\lambda_0} [x \sin(\theta)], \quad (4)$$

where, θ is the deflection angle, λ_0 is the target wavelength, and we set $\lambda_0 = 1540$ nm here. Thus, we get the complete phase distribution in the x direction:

$$\varphi(x, \theta) = \varphi_{Airy}(x) + \varphi_D(x, \theta) \quad (5)$$

is tailored to be suitable angle for propagating Airy beam.

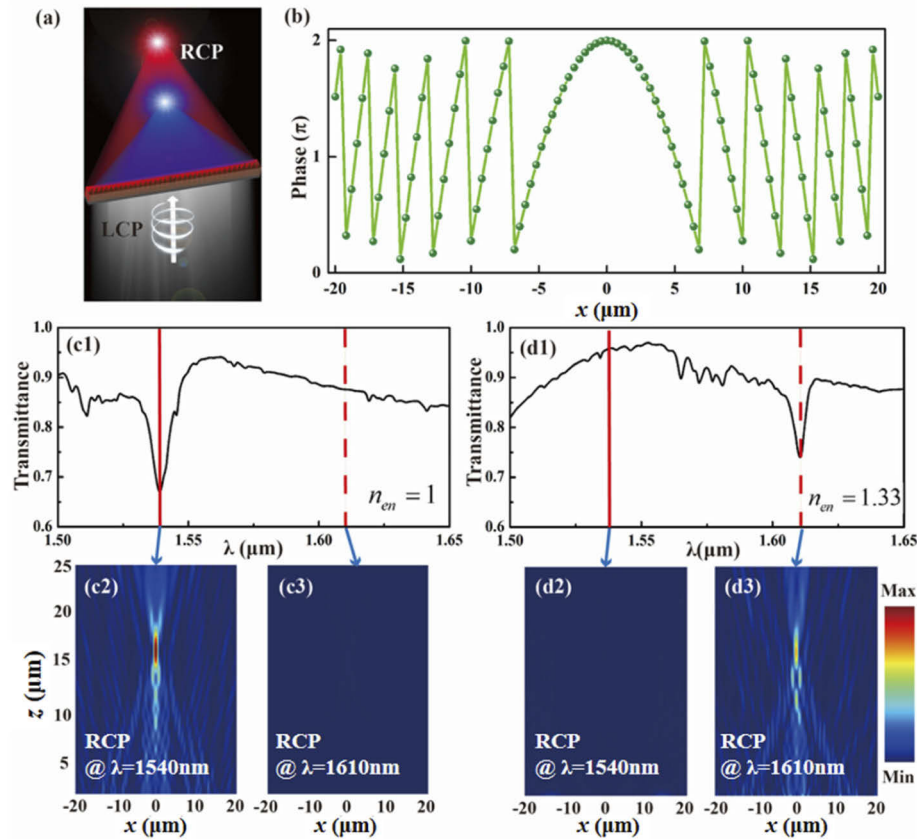


Fig. 4. (a) Schematic of a nonlocal metasurface focuses transmitted light at different wavelength as the variation of environment. (b) The phase profile for focusing the nonlocal metasurface. (c1) Simulated transmittance of the nonlocal metasurface with LCP light normal incident from substrate in the air environment. (c2) and (c3) Simulated intensity of transmitted RCP light at the resonant wavelength of 1540 nm and at the non-resonant wavelength of 1610 nm. (d1) Simulated transmittance of the nonlocal metasurface with LCP light normal incident from substrate in the water environment. (d2) and (d3) Simulated intensity of transmitted RCP light at the non-resonant wavelength of 1540 nm and at the resonant wavelength of 1610 nm.

Figure 5(a) demonstrates the Airy beams generated by nonlocal metasurface with LCP light normal incidence at different resonant wavelength as the variation of surroundings. Figure 5(b) plots the phase distribution of the deflected Airy beam at a distance of $24 \mu\text{m}$ in the x direction, where each dark green ball corresponds to the phase that a unit-cell needs to meet. Figure 5(a) depicts a nonlocal metasurface-based Airy beam generator. If the refractive index of the environmental dielectric is $n_{en} = 1$, such as air, we get the transmission spectrum, as the broad band of LCP light is normal incident from the substrate. Figure 5(c1) shows the simulated transmittance spectrum across a broad communication band. The resonant wavelength is 1540 nm. Figure 5(c2) shows the image of the normalized RCP light intensity which forms an Airy beam. While at a position away from the resonance wavelength, such as 1610 nm, the RCP light does not form an Airy beam, shown as Fig. 5(c3). Then, we set the environmental refractive index $n_{en} = 1.33$, like in water. We can obtain the transmission spectrum curve, as shown in Fig. 5(d1). The resonance wavelength moves from 1540 nm to 1593 nm. Figure 5(d2) and Fig. 5(d3) draw

the normalized RCP light intensity at the non-resonant wavelength of 1540 nm and the resonant wavelength of 1583 nm respectively. As the variation of the environmental index, the wavelength position at which the Airy beam is generated moves from 1540 nm to 1593 nm.

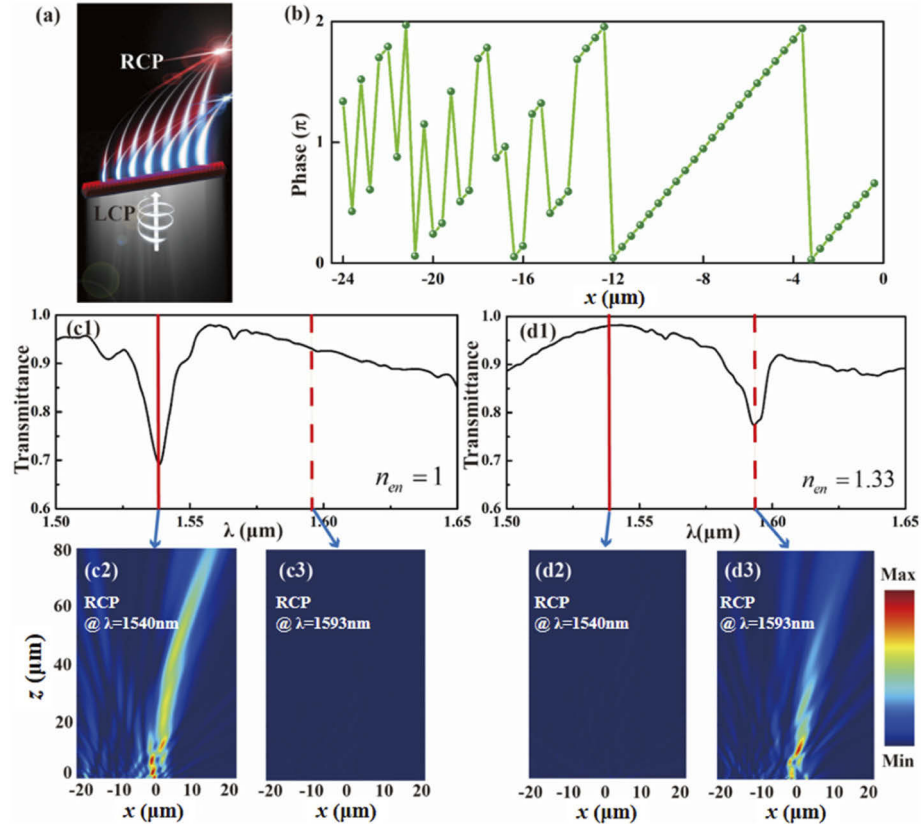


Fig. 5. (a) Schematic of a nonlocal metasurface generates Airy beams at different wavelength as the variation of environment. (b) The phase profile for Airy beam generation. (c1) Simulated transmittance of the nonlocal metasurface with LCP light normal incident from substrate in the air environment. (c2) and (c3) Simulated normalized intensity of transmitted RCP light at the resonant wavelength of 1540 nm and at the non-resonant wavelength of 1593 nm. (d1) Simulated transmittance of the nonlocal metasurface with LCP light normal incident from substrate in the water environment. (d2) and (d3) Simulated normalized intensity of transmitted RCP light at the non-resonant wavelength of 1540 nm and at the resonant wavelength of 1593 nm.

5. Conclusion

In summary, we demonstrated a switchable all-dielectric nonlocal metasurface based on quasi-bound states in the continuum. This device realizes the spatial light manipulation of the narrow band resonant spectrum with adjustable wavelength. We designed a nonlocal metasurface for beam focusing with tunable wavelength in the communication band. We also designed a nonlocal metasurface for the generation of non-diffraction Airy beams with tunable wavelength. This study has potential applications in large-capacity optical communications, nonlinear optics, and imaging.

Funding. Fundamental Research Funds for the Central Universities (020414380175); National Natural Science Foundation of China (11621091, 11774162, 11774164, 11822406, 11834007); National Key Research and Development Program of China (2017YFA0303700).

Acknowledgments. The authors are grateful for the collaborators: Quan Yuan, Xiujuan Zou, Jun Liu, Yifan Wu, Boyan Fu, Xiaoshu Zhu, Guangxing Gong, Ruoyu Lin, Qianhui Bi, Yi Zhang and Mingqian Shi.

Disclosures. The authors declare no conflicts of interest.

Data availability. Data underlying the results presented in this paper are not publicly available at this time but may be obtained from the authors upon reasonable request.

References

1. N. Yu, P. Genevet, M. A. Kats, F. Aieta, J. P. Tetienne, F. Capasso, and Z. Gaburro, "Light propagation with phase discontinuities: generalized laws of reflection and refraction," *Science* **334**(6054), 333–337 (2011).
2. A. Arbabi, Y. Horie, M. Bagheri, and A. Faraon, "Dielectric metasurfaces for complete control of phase and polarization with subwavelength spatial resolution and high transmission," *Nat Nanotechnol* **10**(11), 937–943 (2015).
3. S. Colburn, A. Zhan, and A. Majumdar, "Metasurface optics for full-color computational imaging," *Sci. Adv.* **4**(2), eaar2114 (2018).
4. N. A. Rubin, G. D'Aversa, P. Chevalier, Z. Shi, W. T. Chen, and F. Capasso, "Matrix Fourier optics enables a compact full-Stokes polarization camera," *Science* **365**(6448), 365 (2019).
5. F. Yesilkoy, E. R. Arvelo, Y. Jahani, M. Liu, A. Tittl, V. Cevher, Y. Kivshar, and H. Altug, "Ultrasensitive hyperspectral imaging and biodetection enabled by dielectric metasurfaces," *Nat. Photonics* **13**(6), 390–396 (2019).
6. G. Zheng, H. Muhlenbernd, M. Kenney, G. Li, T. Zentgraf, and S. Zhang, "Metasurface holograms reaching 80% efficiency," *Nat. Nanotechnol.* **10**(4), 308–312 (2015).
7. H. Yu, K. Lee, J. Park, and Y. Park, "Ultrahigh-definition dynamic 3D holographic display by active control of volume speckle fields," *Nat. Photonics* **11**(3), 186–192 (2017).
8. G. Makey, O. Yavuz, D. K. Kesim, A. Turnali, P. Elahi, S. Ilday, O. Tokel, and F. O. Ilday, "Breaking crosstalk limits to dynamic holography using orthogonality of high-dimensional random vectors," *Nat. Photonics* **13**(4), 251–256 (2019).
9. P. Miao, Z. Zhang, J. Sun, W. Walasik, S. Longhi, N. M. Litchinitser, and L. Feng, "Orbital angular momentum microlaser," *Science* **353**(6298), 464–467 (2016).
10. R. C. Devlin, A. Ambrosio, N. A. Rubin, J. P. B. Mueller, and F. Capasso, "Arbitrary spin-to-orbital angular momentum conversion of light," *Science* **358**(6365), 896–901 (2017).
11. C. Spagele, M. Tamagnone, D. Kazakov, M. Ossiander, M. Piccardo, and F. Capasso, "Multifunctional wide-angle optics and lasing based on supercell metasurfaces," *Nat Commun* **12**(1), 3787 (2021).
12. T. Li, X. Xu, B. Fu, S. Wang, B. Li, Z. Wang, and S. Zhu, "Integrating the optical tweezers and spanner onto an individual single-layer metasurface," *Photonics Res.* **9**(6), 1062 (2021).
13. T. Li, X. Li, S. Yan, X. Xu, S. Wang, B. Yao, Z. Wang, and S. Zhu, "Generation and conversion dynamics of dual Bessel beams with a photonic spin-dependent dielectric metasurface," *Phys. Rev. Appl.* **15**(1), 014059 (2021).
14. L. Li, Z. Liu, X. Ren, S. Wang, V. C. Su, M. K. Chen, C. H. Chu, H. Y. Kuo, B. Liu, W. Zang, G. Guo, L. Zhang, Z. Wang, S. Zhu, and D. P. Tsai, "Metalens-array-based high-dimensional and multiphoton quantum source," *Science* **368**(6498), 1487–1490 (2020).
15. Y. Bao, Q. Lin, R. Su, Z. K. Zhou, J. Song, J. Li, and X. H. Wang, "On-demand spin-state manipulation of single-photon emission from quantum dot integrated with metasurface," *Sci. Adv.* **6**(31), eaba8761 (2020).
16. H. Kwon, D. Sounas, A. Cordaro, A. Polman, and A. Alu, "Nonlocal metasurfaces for optical signal processing," *Phys. Rev. Lett.* **121**(17), 173004 (2018).
17. A. Overvig and A. Alù, "Wavefront-selective Fano resonant metasurfaces," *Adv. Photonics* **3**(02), 3 (2021).
18. A. C. Overvig, S. C. Malek, and N. Yu, "Multifunctional nonlocal metasurfaces," *Phys. Rev. Lett.* **125**(1), 017402 (2020).
19. Jung-Hwan Song, Jorik van de Groep, Soo Jin Kim, and M. L. Brongersma, "Nonlocal metasurfaces for spectrally decoupled wavefront manipulation and eye tracking," arXiv:2102.05790 (2021).
20. Stephanie C. Malek, Adam C. Overvig, Andrea Alù, and N. Yu, "Resonant wavefront-shaping flat optics," arXiv:2009.07054 (2020).
21. A. M. Shaltout, V. M. Shalaev, and M. L. Brongersma, "Spatiotemporal light control with active metasurfaces," *Science* **364**(6441), 364 (2019).
22. A. She, S. Zhang, S. Shian, D. R. Clarke, and F. Capasso, "Adaptive metalenses with simultaneous electrical control of focal length, astigmatism, and shift," *Sci. Adv.* **4**(2), eaap9957 (2018).
23. B. Xiong, Y. Xu, J. Wang, L. Li, L. Deng, F. Cheng, R. W. Peng, M. Wang, and Y. Liu, "Realizing colorful holographic mimicry by metasurfaces," *Adv. Mater.* **33**(21), 2005864 (2021).
24. Stephanie C. Malek, Adam C. Overvig, Sajjan Shrestha, and N. Yu, "Active nonlocal metasurfaces," arXiv:2008.09141 (2020).
25. C. W. Hsu, B. Zhen, A. D. Stone, J. D. Joannopoulos, and M. Soljačić, "Bound states in the continuum," *Nat. Rev. Mater.* **5**(9), e16147 (2016).

26. K. Koshelev, S. Lepeshov, M. Liu, A. Bogdanov, and Y. Kivshar, "Asymmetric metasurfaces with high-Q resonances governed by bound states in the continuum," *Phys. Rev. Lett.* **121**(19), 193903 (2018).
27. H. Zhou, B. Zhen, C. W. Hsu, O. D. Miller, S. G. Johnson, J. D. Joannopoulos, and M. Soljačić, "Perfect single-sided radiation and absorption without mirrors," *Optica* **3**(10), 1079–1086 (2016).
28. C. W. Hsu, B. Zhen, J. Lee, S. L. Chua, S. G. Johnson, J. D. Joannopoulos, and M. Soljacic, "Observation of trapped light within the radiation continuum," *Nature* **499**(7457), 188–191 (2013).
29. A. C. Overvig, S. C. Malek, M. J. Carter, S. Shrestha, and N. Yu, "Selection rules for quasibound states in the continuum," *Phys. Rev. B* **102**(3), 035434 (2020).
30. M. V. Berry and N. L. Balazs, "Nonspreading wave packets," *Am. J. Phys.* **47**(3), 264–267 (1979).
31. G. A. Siviloglou, J. Broky, A. Dogariu, and D. N. Christodoulides, "Observation of accelerating Airy beams," *Phys. Rev. Lett.* **99**(21), 213901 (2007).
32. T. Vettenburg, H. I. Dalgarno, J. Nylk, C. Coll-Llado, D. E. Ferrier, T. Cizmar, F. J. Gunn-Moore, and K. Dholakia, "Light-sheet microscopy using an Airy beam," *Nat Methods* **11**(5), 541–544 (2014).
33. S. Jia, J. C. Vaughan, and X. Zhuang, "Isotropic 3D super-resolution imaging with a self-bending point spread function," *Nat Photonics* **8**(4), 302–306 (2014).
34. J. Baumgartl, M. Mazilu, and K. Dholakia, "Optically mediated particle clearing using Airy wavepackets," *Nat. Photonics* **2**(11), 675–678 (2008).
35. A. Chong, W. H. Renninger, D. N. Christodoulides, and F. W. Wise, "Airy–Bessel wave packets as versatile linear light bullets," *Nat. Photonics* **4**(2), 103–106 (2010).
36. Y. Liang, Y. Hu, D. Song, C. Lou, X. Zhang, Z. Chen, and J. Xu, "Image signal transmission with Airy beams," *Opt. Lett.* **40**(23), 5686–5689 (2015).